Materials Science & Engineering A 625 (2015) 380–384

Contents lists available at ScienceDirect

Materials Science & Engineering A

journal homepage: www.elsevier.com/locate/msea

High temperature indentation of helium-implanted tungsten

James S.K.-L. Gibson [a,*], Steve G. Roberts [a,b], David E.J. Armstrong [a]

[a] Oxford University, Department of Materials, Parks Road, Oxford OX1 3PH, UK
[b] Culham Centre for Fusion Energy, Culham Science Centre, Abingdon OX14 3DB, UK

ARTICLE INFO

Article history:
Received 8 October 2014
Received in revised form
5 December 2014
Accepted 8 December 2014
Available online 18 December 2014

Keywords:
Hardness measurement
Nanoindentation
Hardening

ABSTRACT

Nanoindentation has been performed on tungsten, unimplanted and helium-implanted to ~600 appm, at temperatures up to 750 °C. The hardening effect of the damage was 0.90 GPa at 50 °C, but is negligible above 450 °C. The hardness value at a given temperature did not change on re-testing after heating to 750 °C. This suggests that the helium is trapped in small vacancy complexes that are stable to at least 750 °C, but which can be bypassed due to increased dislocation mobility (cross slip or climb) above 450 °C.

1. Introduction

As the main plasma-facing material in a fusion reactor [1], tungsten will be exposed to a flux of alpha particles (essentially helium ions) from the plasma as well as 14 MeV neutrons. While the rate of helium production due to transmutation is negligible, this incident alpha particle flux will result in a high concentration of diffused-in helium that may combine with displacement damage from incident neutrons. The resulting defects are likely to produce significant mechanical property changes. There have been several studies on tungsten and tungsten alloys using neutrons or self-ion irradiations, in conjunction with either micro-indentation [2–4], nanoindentation [5,6] or micro-bending [7] experiments to probe the effect that displacement damage has on mechanical properties, such as hardness or yield stress. However all these studies have produced data at room temperature only; they also considered only the effects of displacement damage on mechanical behaviour and not any additional effects that helium might have.

Research into the effects of helium on tungsten has mainly focussed on determining the lattice position helium occupies at very low concentrations [8] and characterisation of 'nanofuzz' structures formed under conditions of high flux [9]. With regard to mechanical properties, work by Armstrong et al. [10] demonstrated the considerable hardening effect of helium in tungsten at room temperature even at relatively low concentrations (300 appm). Beck et al. [11] showed a similar hardening effect of implanted helium in tungsten–rhenium and tungsten–tantalum alloys. Beck also used TEM to show that the implanted helium does not form visible bubbles even at concentrations of approximately 3000 appm, suggesting that the implanted helium is in solution, or sits in stable vacancy-helium clusters below the resolution limit of the TEM.

However, in both Armstrong's and Beck's works the helium implantation took place at 300 °C, and mechanical properties were measured at room temperature. The expected steady state operating temperatures of tungsten are up to 700 °C at the first wall and up to 500 °C in the divertor [12]. During operation, these components will also be subject to fast neutron irradiation, producing displacement damage at a typical rate of 15 dpa/FPY [13]. As vacancy mobility becomes significant above 530 °C in tungsten [14], this will likely have an effect on the damage structures formed by the helium ions as well as the mechanical properties above this temperature.

This work aims to study pure tungsten (investigated previously [15,16]) implanted with helium ions at a reactor-relevant temperature of 800 °C. It also extends nanoindentation methods typically used to study effects of radiation damage [5] to tests performed at elevated temperatures, up to the 750 °C expected during standard service conditions. This is important to determine the mechanical properties of components during reactor operations, and also to study the hardening mechanisms that may influence component brittleness during maintenance periods.

2. Experimental methods

2.1. Ion implantation

Commercially pure tungsten (MCO, Cambridge, UK) was irradiated at 800 °C using 2 MeV He^+ ions at JANNuS (CEA Saclay, France) with a

* Corresponding author. Tel.: +44 1865 273767.
E-mail address: james.gibson@materials.ox.ac.uk (J.-L. Gibson).

http://dx.doi.org/10.1016/j.msea.2014.12.034

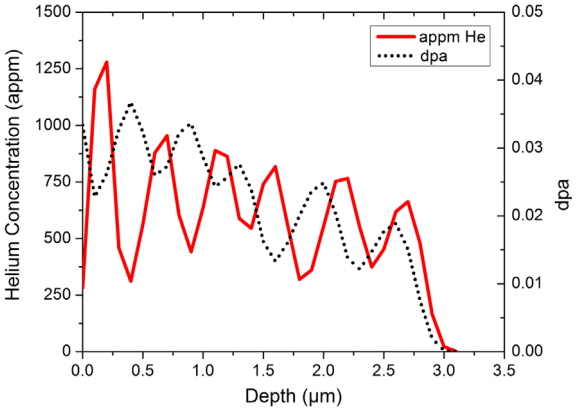

Fig. 1. Helium distribution and dpa profile in the ion-implanted later as predicted using SRIM-2008 (Stopping Range of Ions in Matter). The 'quick' Kinchin–Pease calculation of damage was used with a displacement energy of 68 eV. This gives an average concentration of 600 appm in the 3 μm implanted region. The multiple peaks were generated by implantation through a series of degrader foils from 0 to 6 μm.

series of aluminium degrader foils in place to produce the predicted depth distribution shown in Fig. 1. A dose of 1.21×10^{16} ions cm^{-2} was implanted at a flux of 7.51×10^{11} ions $cm^{-2}s^{-1}$. Five degrader foils (6 μm, 5 μm, 4 μm, 3 μm and 1.6 μm) were used in addition to the un-degraded 2 MeV beam. The profile has a peak concentration of 1250 appm at 0.15 μm depth, with an average concentration of 600 appm over the total depth of 3 μm. The temperature was monitored using a thermocouple mounted just behind the samples in the sample holder, and an infrared camera was used to check that a uniform temperature profile across the sample was achieved. Beam currents were measured periodically using a set of four Faraday cups.

Previous work on tungsten implanted with helium of the same energy range [10] used continuous stiffness measurement nanoindentation [17] to determine the depth to which nanoindentation results are unaffected by the unimplanted substrate. This analysis showed that values of hardness extracted < 400 nm into the surface are dominated by the ion-implanted layer, while hardness values extracted from > 1500 nm into the surface are dominated by the hardness of the bulk material. These critical depths are used here in the analysis of the load-unload data at high temperatures.

2.2. High temperature micro-indentation

High temperature micro-indentation has been widely used to study the hardness dependence on temperature on a variety of materials. In the case of tungsten there is a well-documented "knee" in the hardness drop at around 300 °C, where the rate of change in hardness significantly decreases [18,19]. To study the accuracy of the high temperature nanoindentation experiments, high temperature micro-hardness tests were performed over the same temperature range. A single-crystal sample of tungsten from the same source used for the nanoindentation study was used. Indentations were performed using a sapphire Vickers indenter and a 200 g load held for 15 s to allow for any indentation creep effects. Five indents were performed at each temperature from 23 °C to 700 °C

2.3. High temperature nano-indentation

High temperature nanoindentation was performed on an unirradiated sample and a helium-implanted sample using a MicroMaterials NanoTest nanoindenter. This instrument is housed in a vacuum chamber that attains a vacuum level of $< 10^{-5}$ mbar. A cubic boron nitride indenter with standard Berkovich geometry was used. Tungsten samples were mounted on a furnace using FortaFix Autostic FC6 high temperature cement. A thermocouple was cemented to the surface of the sample to monitor the temperature of the material in contact with the indenter. A second thermocouple in the indenter was used to equalise sample and indenter temperatures during the indentation process. At least 36 indents were performed at each temperature. Each indent was performed using twenty load-unload segments, evenly distributed in depth from 50 to 2000 nm so as to determine hardness as a function of depth. This produces load–displacement curves as shown in Fig. 2. The form of the curves – apart

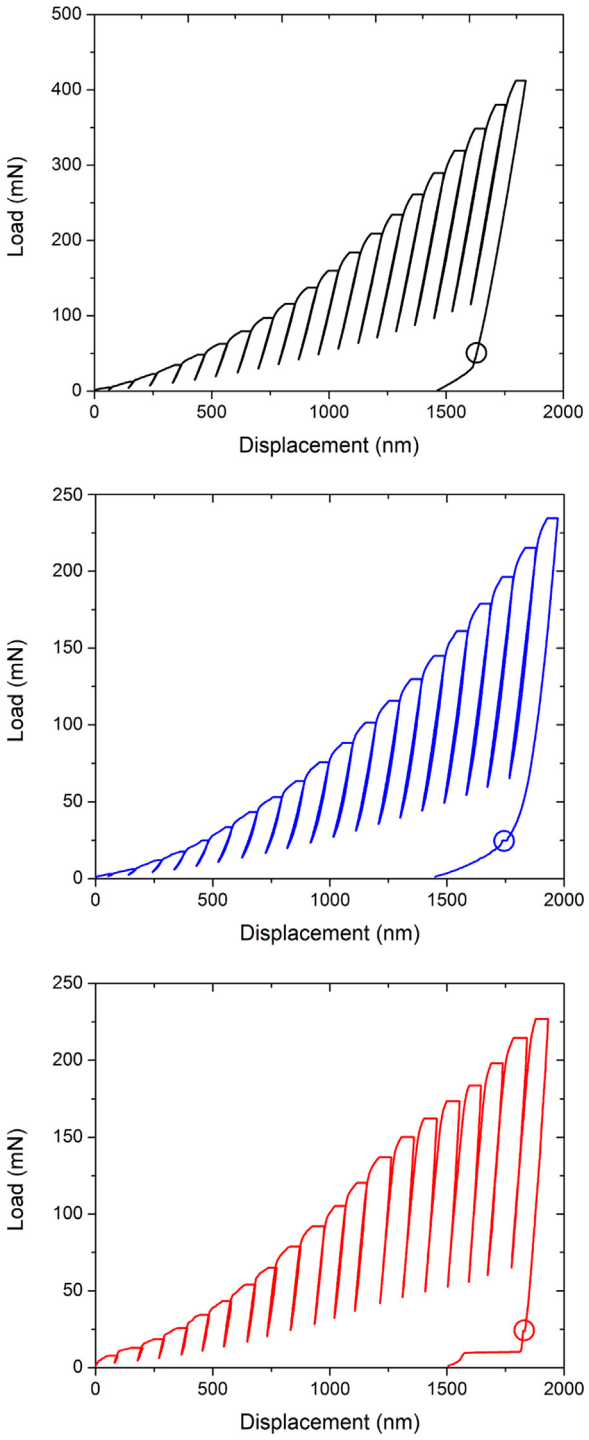

Fig. 2. Typical load–partial unload curves for indents performed at 50 °C (black), 350 °C (blue) and 750 °C (red). No differences in form – except for the peak load – are seen between the three curves. Post-indentation drift is measured at 80% unload; these regions are circled on the curves. (For interpretation of the references to colour in this figure legend, the reader is referred to the web version of this article.)

from the peak load – is the same at all temperatures. Loading and unloading were conducted at a rate of 1.5 mN/s, with a 15 s hold at the peak load for each cycle. Prior to the start of each indentation, the tip was brought into contact with the sample for 120 s in a thermalisation step. Drift rates were measured over a 60 s hold at 30% of the peak load; both before indentation (after the thermalisation step) and after the final unload cycle.

Samples were heated from 50 °C to 750 °C in 100 °C increments, with at least 36 indents performed at each temperature. The sample was heated at a rate of 2 °C/min. The system was then left to stabilise at each temperature for at least six hours before performing tests. After indents had been made at 750 °C, the sample was cooled at 2 °C/min and indentation was also performed at 550 °C, 350 °C, 50 °C and 20 °C. At each of these temperatures the six-hour stabilisation was also carried out. This was done to assess the hardening behaviour after the sample had been held at an elevated temperature, to investigate the stability of the helium-induced damage.

It is necessary to minimise thermal drift in the system in order to produce accurate data, especially for the long contact times (~25 min) required for a complete load–partial unload indentation cycle. A thermal fluctuation of 1 °C can lead to a drift displacement of ~100 nm [20].

Temperature matching was accomplished by matching the temperature measured by the indenter thermocouple with that measured by the thermocouple mounted to the sample to within 1 °C before testing. This was done with the tip in close proximity (< 20 μm) to the sample. At these distances, the tip temperature is strongly influenced by radiative heating from the sample. In order to produce a stable tip temperature and prevent drift during the experiment, the input power from the heater must balance the contributions from both the radiative heating and conduction when the tip is in contact with the sample. The temperature-matching process is further complicated due to the tip thermocouple being positioned closer to the heater than the actual Berkovich tip, leading to uncertainty in the actual tip temperature.

A series of trial indents was thus performed in order to confirm temperature stability by measuring drift rates and observing the shape of the load–displacement curve. If drift levels were too high, the tip temperature was varied based on the measured drift rates and more trial indents were performed to check the drift rates. Once stability was confirmed within the system, the array of load-partial unload tests was made.

Fig. 3 shows typical thermal drift data obtained before indentation at 50 °C, 350 °C and 750 °C, demonstrating the tight control of drift. Table 1 shows the average pre- and post-indentation drift rates for all the tests performed. This was chosen as the best measurement of drift as it shows the thermal stability of the system over the course of the full indentation experiment. The drift data collected post-indentation were extremely close to drift data collected pre-indentation. Indentation in vacuum significantly increases thermal drift, due to the lack of convection to equilibrate temperatures between sample and indenter. The authors believe these drift rates to be amongst the lowest achieved in high-temperature indentation [21].

Table 1
Thermal drift analysis for average (pre- and post-indentations) drift rates for the helium-implanted sample.

Temperature (°C)	Number of indents	% of Indentations with drift		
		< 0.15 nm/s	< 0.10 nm/s	< 0.05 nm/s
50	42	100	100	62
150	39	100	100	97
250	39	97	95	51
350	75	99	92	57
450	36	100	64	6
550	36	89	67	39
650	45	96	89	64
750	60	93	78	58

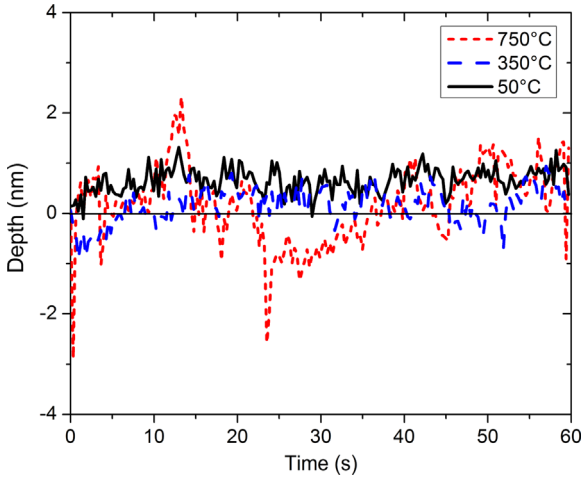

Fig. 3. Pre-indentation thermal drift data for indents performed at 50 °C and 750 °C. The 750 °C indentation shows greater scatter, but all drift rates are below 0.01 nm/s.

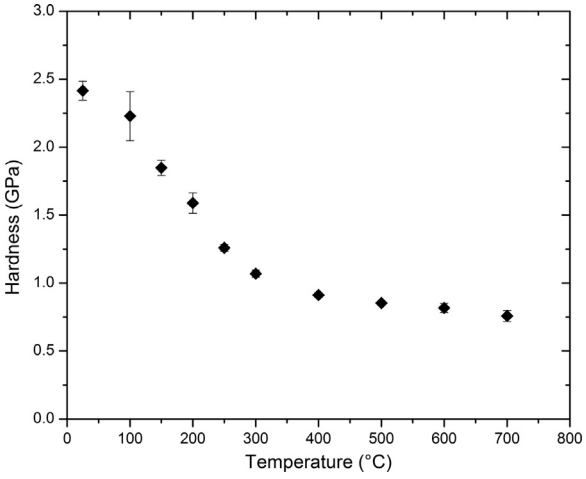

Fig. 4. Microindentation hardness of tungsten as a function of temperature. Two distinct regions, above and below ≈300 °C can be seen. Error bars indicate one standard deviation in the measured hardness.

3. Results

Fig. 4 shows the variation of micro-hardness as a function of temperature. A steep initial drop in hardness is seen up to 300 °C with an average hardness decrease of 5 MPa/ °C, (a decrease to 45% of the 20 °C hardness value over 280 °C). Above 300 °C the rate of hardness change significantly decreases to 0.7 MPa/ °C. These data are in good agreement with high temperature micro-hardness experiments performed by Lee and Flom [18] and Pisarenko [19] who saw a similar rate of change of hardness in the same temperature regimes.

Fig. 5 shows results from nanoindentation tests. The values of hardness shown were calculated as the means of hardness from each partial unload over all indents at a given temperature. 'Surface' data are the average value of hardness for data collected between 150 and 400 nm depth. This samples only the implanted

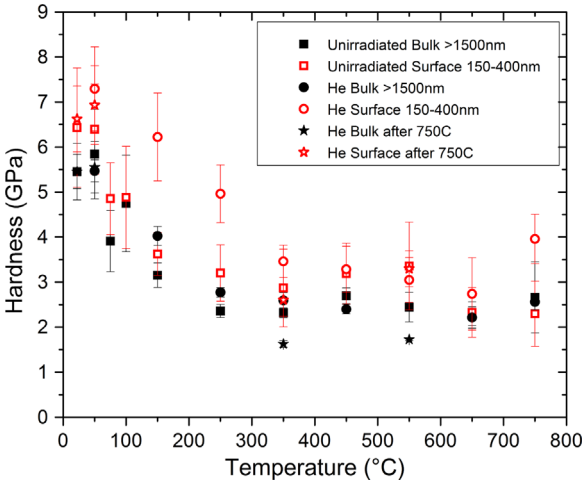

Fig. 5. Nanoindentation hardness as a function of temperature. Points denoted with a star indicate data obtained on cooling after the indentations performed at 750 °C. Error bars indicate one standard deviation in the measured hardness.

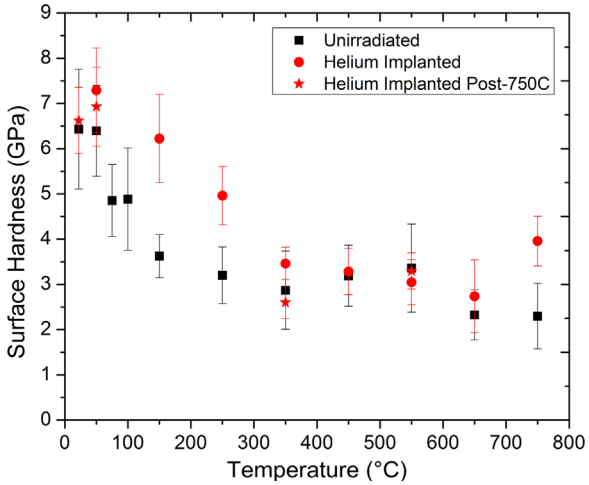

Fig. 6. Nanoindentation hardness from shallow indents ('surface' data in Fig. 5) for an unirradiated sample and the helium-implanted sample.

layer, but avoids the significant size effects that would be present below 150 nm depth [5,22]. 'Bulk' values were determined in the same way for data collected at depths greater than 1500 nm.

For unimplanted tungsten, the hardness of the bulk material decreases rapidly from 5.5 GPa at 20 °C to 2.5 GPa at 150 °C (a decrease to 45% of the 20 °C hardness value over 130 °C), and then is constant up to 750 °C. The absolute hardness values are higher from nanoindentation than for microindentation, but the transition between the rapid decrease in hardness and a plateau region is still seen at 300 °C. The relative rate of change in hardness with temperature is 11 MPa/ °C for the initial drop, and 0.3 MPa/ °C above 300 °C. The difference in the absolute values is most likely due to the difference in mechanical behaviour between single-crystal tungsten tested in the micro-indentation and polycrystalline tungsten tested in the nanoindentation. However, these data show that there is a significant change in rate of hardness change regardless of sample microstructure above ~300 °C, around the temperature at which the hardening from the helium implantation becomes negligible.

There is a size effect in the unimplanted material: the hardness of the material 150–400 nm from the surface is on average 16% (~0.5 GPa) harder than the data >1500 nm in depth, assuming the Nix-Gao relationship holds true and the size effect is a multiplicative effect [22].

The values of hardness from the >1500 nm depth load-unload curves for irradiated and unirradiated material match closely. This shows the validity of the conclusion from room temperature data; that the hardness derived from data >1500 nm in depth has little influence from the implanted layer. It also shows the reproducibility of the results, and that any effects of thermal drift are minimal between different samples.

The hardening effect of the implanted helium, visible from in the data from 150 to 400 nm depths (Fig. 6 and Table 2), is up to 2.5 GPa at low temperatures, a significant increase in hardness. The hardening effect decreases with increasing temperature and is not significantly present above 450 °C. When the sample is cooled from 750 °C and indents are performed during the cooling cycle, the hardening effect is the same at a given temperature as for tests performed during the heating cycle.

Table 2
Nanoindentation hardness as a function of temperature, with the increase in hardness from helium-implantation calculated.

Temperature (°C)	Unimplanted hardness (GPa)	He-implanted hardness (GPa)	Δ Hardness (GPa)
50	6.39	7.29	0.90
250	3.20	4.96	1.76
450	3.19	3.28	0.09
650	2.33	2.74	0.41

4. Discussion

If the decrease in the hardening effect of implanted helium at high temperature was due to helium desorption from the implanted layer or helium diffusion into the bulk, then the permanently-induced reduction in obstacle density or strength would result in a lower hardness at a given temperature on cooling compared to the values measured on the heating cycle. Since near-surface hardness values are the same at a given temperature on both heating and cooling cycles, the decrease in hardness with increasing temperature in the helium-implanted sample must be due to the helium-vacancy complexes generated during ion implantation becoming weaker obstacles to plastic deformation at increased temperatures, rather than to any thermal removal of helium or damage.

This implied retention of the helium up to 750 °C matches with results from thermal desorption spectroscopy (TDS) of tungsten implanted with high-energy helium ions [23]. The TDS showed that helium is trapped in mono-vacancies and helium-vacancy clusters up until ~1200 to 1300 °C. This conclusion is supported by TEM of helium-implanted tungsten that shows no visible bubbles at He concentrations up to 3000 appm, suggesting the helium is trapped in defects below the resolution limit of the microscope [11]. Finally, DFT modelling of helium in tungsten [24] shows almost complete stability of $He_n v_m$ clusters ($0 \le n \le 4$, $0 \le m \le 4$) at temperatures up to ~400 °C.

MD simulation indicates that the critical resolved shear stress for an edge dislocation to un-pin from a helium-vacancy complex in α-Fe decreases only by ~10% between 100 K and 600 K [25]. This is unlikely to be significant enough to explain the ~50% drop in hardening seen here. Therefore, the majority of the drop is more likely to be due to thermally-activated mechanisms for dislocations to bypass such obstacles: increased mobility and cross-slip of screw dislocations [26] and climb of edge dislocations [27]. The low damage levels produced during the implantation (~0.2 dpa) and relatively high helium levels (~600 appm) are likely to favour the production of small defects that become easy to overcome via cross-slip and climb as temperature increases, especially as these

defects cannot be seen in the TEM [11]. It is clear that the mobility of dislocations increases over this temperature range due to the significant drop in hardness of tungsten seen in the micro-indentation curve, and macro-indentation [19].

The strength of the helium-vacancy clusters can be estimated by calculating the critical angle for dislocation breakaway during glide (ϕ_c), which is given by Eq. 1 [28]. G is the bulk modulus (161 GPa), b the Burgers vector (0.22 nm), L is the obstacle spacing, $\Delta\tau$ is the change in shear yield stress due to obstacles (approximately one sixth of the hardness change).

$$\phi_c = 2\ \cos^{-1}\left(\frac{G\,b}{L\,\Delta\tau}\right) \quad (1)$$

To a first approximation, the obstacle spacing is given by the cube root of the inverse of the obstacle density. If it is assumed that the 600 appm helium sits in small He_nv_m clusters (with $n<4$) (as the high irradiation temperature favours large complexes with lower helium content when compared to low temperatures where vacancies are not mobile [29]), the obstacle density may be calculated by distributing 600 helium atoms among 5×10^5 tungsten unit cells (each containing two tungsten atoms) each of volume 3.16×10^{-29} m^{-3}. For $1<n<4$, ϕ_c varies between 172° and 175°, i.e. each helium-vacancy cluster is an extremely weak obstacle. Thus the strengthening effect of the obstacles arising from helium implantation is due to the presence of a very high density of relatively weak obstacles. The rapid drop in irradiation-induced hardening with increasing temperature may be due to the already low obstacles strength falling to negligible values as thermally activated bypass mechanisms become increasingly operative.

Other data on high temperature micro-deformation of BCC materials is sparse. Schneider et al. [30] performed high temperature micro-pillar compression tests in molybdenum at 300 K and 500 K; these temperatures being chosen to be below and above the reported critical temperature for screw dislocation mobility in molybdenum. They observed a significant decrease in yield stress as temperature was increased, in pillars ranging from 0.5 μm to 5 μm diameter, with smaller pillars being less sensitive to temperature. Recent work by Torrents et al. [31] involved similar micro-pillar compression experiments in tungsten from room temperature to 400 °C. They also observed a decrease in yield stress as temperature was increased: similarly to molybdenum [30], the sensitivity to temperature was lower in smaller diameter pillars. This size effect on temperature dependence of yield behaviour was attributed to the easy nucleation of kinks on screw dislocations at the pillar surface; this being more significant in smaller diameter pillars. However, with the significantly higher strains and work-hardening under Berkovitch indents compared to micro-pillar experiments, it is difficult to directly compare the types of experiments.

5. Conclusion

Micro- and nano- indentations have been performed on unimplanted and helium-implanted tungsten at temperatures up to 750 °C. The measured drift rates in high-temperature nanoindentation are extremely low, allowing quantitative measurements of hardness to be obtained with trends that match well with micro-hardness measurements. In unimplanted material, hardness falls to ~45% of the room temperature value at 150–300 °C, above which, hardness decreases only very slowly with increasing temperature. The implanted helium is trapped up to the highest test temperature (750 °C), probably in the form of helium-vacancy clusters. The hardening effect of the irradiation damage was 0.90 GPa at 50 °C, but is negligible above 450 °C. This decrease in irradiation hardening with temperature is most likely due to the increased ability of dislocations to bypass small, irradiation-induced obstacles due to the increased frequency of cross-slip and climb.

Acknowledgements

The work reported here was supported by the EPSRC via the programme Grant “Materials for Fusion and Fission Power”, (EP/H018921). We are also grateful for the financial support of the Royal Academy of Engineering (DEJA) and the Culham Centre for Fusion Energy (JSK-LG). Our thanks to the staff at CEA and SPIRIT funding for the ion implantation.

References

[1] H. Bolt, V. Barabash, W. Krauss, J. Linke, R. Neu, S. Suzuki, N. Yoshida, J. Nucl. Mater. 329–333 (2004) 66–73.
[2] M. Fukuda, A. Hasegawa, T. Tanno, S. Nogami, H. Kurishita, J. Nucl. Mater. 442 (2013) S273–S276.
[3] M. Fukuda, T. Tanno, S. Nogami, A. Hasegawa, Mater. Trans. 53 (2012) 2145–2150.
[4] T. Tanno, A. Hasegawa, J.C. He, M. Fujiwara, S. Nogami, M. Satou, T. Shishido, K. Abe, Mater. Trans. 48 (2007) 2399–2402.
[5] D.E.J. Armstrong, X. Yi, E.A. Marquis, S.G. Roberts, J. Nucl. Mater. 432 (2013) 428–436.
[6] D.E.J. Armstrong, A.J. Wilkinson, S.G. Roberts, Phys. Scr. T145 (2011).
[7] J. Gibson, D. Armstrong, S. Roberts, Phys Scr. T159 (2014).
[8] C.S. Becquart, C. Domain, Nucl. Instrum. Methods Phys. Res. Sect. B 255 (2007) 23–26.
[9] M.J. Baldwin, R.P. Doerner, J. Nucl. Mater. 404 (2010) 165–173.
[10] D.E.J. Armstrong, P.D. Edmondson, S.G. Roberts, Appl. Phys. Lett. 102 (2013).
[11] C.E. Beck, S.G. Roberts, P.D. Edmondson, D.E.J. Armstrong, MRS Fall Meeting, Boston, MA, 2013, pp. 99–104.
[12] H. Bolt, V. Barabash, G. Federici, J. Linke, A. Loarte, J. Roth, K. Sato, J. Nucl. Mater. 307–311 (2002) 43–52.
[13] M.R. Gilbert, S.L. Dudarev, D. Nguyen-Manh, S. Zheng, L.W. Packer, J.C. Sublet, J. Nucl. Mater. (2013) S755–S760.
[14] T. Tanno, M. Fukuda, S. Nogami, A. Hasegawa, Mater. Trans. 52 (2011) 1447–1451.
[15] A. Giannattasio, S.G. Roberts, Philos. Mag. 87 (2007) 2589–2598.
[16] A. Giannattasio, Z. Yao, E. Tarleton, S.G. Roberts, Philos. Mag. 90 (2010) 3947–3959.
[17] X. Li, B. Bhushan, Mater. Charact. 48 (2002) 11–36.
[18] M.Y. Lee, D.G. Flom, J. Am. Ceram. Soc. 73 (1990) 2117–2118.
[19] G.S. Pisarenko, V.A. Borisenko, Y.A. Kashtalyan, Powder Metall. Met. Ceram. 1 (1964) 371–374.
[20] C.A. Schuh, C.E. Packard, A.C. Lund, J. Mater. Res. 21 (2006) 725–736.
[21] S. Korte, R.J. Stearn, J.M. Wheeler, W.J. Clegg, J. Mater. Res. 27 (2012) 167–176.
[22] W.D. Nix, H. Gao, J. Mech. Phys. Solids 46 (1998) 411–425.
[23] P.E. Lhuillier, A. Debelle, T. Belhabib, A.L. Thomann, P. Desgardin, T. Sauvage, M.F. Barthe, P. Brault, Y. Tessier, J. Nucl. Mater. 417 (2011) 504–507.
[24] A. Rivera, G. Valles, M.J. Caturla, I. Martin-Bragado, Nucl. Instrum. Methods Phys. Res. Sect. B 303 (2013) 81–83.
[25] L. Yang, Z.Q. Zhu, S.M. Peng, X.G. Long, X.S. Zhou, X.T. Zu, H.L. Heinisch, R.J. Kurtz, F. Gao, J. Nucl. Mater. 441 (2013) 6–14.
[26] J. Cheng, S. Nemat-Nasser, W. Guo, Mech. Mater. 33 (2001) 603–616.
[27] Y.N. Osetsky, D.J. Bacon, Philos. Mag. 90 (2010) 945–961.
[28] W. Soboyejo, Mechanical Properties of Engineered Materials, CRC Press, USA, 2002 (ISBN 0-8247-8900-8).
[29] X. Ou, W. Anwand, R. Kögler, H.B. Zhou, A. Richter, J. Appl. Phys. 115 (2014) 123521.
[30] A.S. Schneider, C.P. Frick, E. Arzt, W.J. Clegg, S. Korte, Philos. Mag. Lett. 93 (2013) 331–338.
[31] O. Torrents, J.M. Wheeler, J. Michler, E. Arzt, A.S. Schneider, Personal Communication, 2014.